Complete title:

Quantitative analysis of cation mixing and local valence states in $LiNi_xMn_{2-x}O_4$ using concurrent HARECXS and HARECES measurements

Running title:

HARECX(E)S analyses of LIB cathode materials

Contributors:

Yu Yamamoto

Sumika Chemical Analysis Service, Ltd., 6 Kitahara, Tsukuba, Ibaraki 300-3266, Japan

Department of Materials, Physics and Energy Engineering, Nagoya University, Furo-cho, Chikusa-ku, Nagoya, Aichi 464-8603, Japan

Tel.: +81 29 864 4741

Fax: +81 29 864 4085

E-mail: yuu.yamamoto@scas.co.jp

Kunimitsu Kataoka

National Institute of Advanced Industrial Science and Technology (AIST), Central 5, 1-1-1 Higashi, Tsukuba, Ibaraki 305-8565, Japan

Tel.: +81 29 861 3337

Fax: +81 29 861 9214

E-mail: kataoka-kunimitsu@aist.go.jp

Junji Akimoto

National Institute of Advanced Industrial Science and Technology (AIST), Central 5, 1-1-1

Higashi, Tsukuba, Ibaraki 305-8565, Japan

Tel.: +81 29 861 4408

Fax: +81 29 861 9214

E-mail: j.akimoto@aist.go.jp

Kazuyoshi Tatsumi

EcoTopia Science Institute, Nagoya University, Furo-cho, Chikusa-ku, Nagoya, Aichi 464-8603, Japan

Tel.: +81 52 789 5135

Fax: +81 52 789 5137

E-mail: k-tatsumi@nucl.nagoya-u.ac.jp

Takashi Kousaka

Sumika Chemical Analysis Service, Ltd., 6 Kitahara, Tsukuba, Ibaraki 300-3266, Japan

Tel.: +81 29 864 4741

Fax: +81 29 864 4085

E-mail: kousaka@scas.co.jp

Jun Ohnishi

Sumika Chemical Analysis Service, Ltd., 1-7-5 Kikumoto, Niihama, Ehime 792-0801, Japan

Tel.: +81 89 734 2845

Fax: +81 89 732 8291

E-mail: j.onishi@scas.co.jp

Teruo Takahashi

Sumika Chemical Analysis Service, Ltd., 6 Kitahara, Tsukuba, Ibaraki 300-3266, Japan

Tel.: +81 29 864 4741

Fax: +81 29 864 4085

E-mail: teruo.takahashi@scas.co.jp

Shunsuke Muto

EcoTopia Science Institute, Nagoya University, Furo-cho, Chikusa-ku, Nagoya, Aichi 464-8603, Japan

Tel.: +81 52 789 5200

Fax: +81 52 789 5137

E-mail: s-mutoh@nucl.nagoya-u.ac.jp

Keywords:

Lithium ion secondary batteries

Positive electrode materials

Cation mixing

Site-specific EELS

Electron channeling

Multiple linear regression

Total number of pages: 31

Total number of figures: 7

Abstract

Cation mixing in positive electrode materials for rechargeable lithium ion batteries, $LiNi_xMn_{2-x}O_4$ (x = 0, 0.2, 0.5) and $Li_{0.21}Ni_{0.7}Mn_{1.64}O_{4-\delta}$ (denoted as x = 0.7) is analyzed by high-angular-resolution electron-channeling X-ray/electron spectroscopy (HARECXS/HARECES) techniques, using energy-dispersive X-ray spectroscopy and electron energy-loss spectroscopy. Mixing between the tetrahedral lithium sites and the octahedral transition metal sites is quantified, and the site-dependent valence states of the transition metals are examined. In the non-doped (x = 0) sample, Mn was found to occupy only octahedral sites as either Mn^{3+} or Mn^{4+}. For x = 0.2–0.7, some of the nickel ions (6–13% depending on x) occupy tetrahedral anti-sites. All the nickel ions are in the divalent state, regardless of the occupation site. For x = 0.2 and 0.7, manganese ions occupy both octahedral and tetrahedral sites; those in the octahedral sites are tetravalent, while the tetrahedral sites contain a mixture of divalent and trivalent ions. For x = 0.5, manganese occupies only the octahedral sites, with all ions determined to be in the tetravalent state (within experimental accuracy). All the samples substantially satisfied the local charge neutrality conditions. This study demonstrates the feasibility of using HARECXS/HARECES for quantitative analysis of the atomic configuration and valence states in lithium manganese oxide spinel materials.

Introduction

Electron channeling in a crystalline material occurs when an incident electron beam propagates along particular atomic planes/columns, and the channeling effect depends on the direction of the beam with respect to the crystal axes. The site-specific energy-dispersive X-ray (EDX) analysis technique that takes advantage of electron channeling effects is known as the atom location by channeled electron microanalysis (ALCHEMI) method [1–3], and is

used to evaluate the fraction of host atomic sites occupied by impurities. This method has been extended in a more sophisticated and quantitatively reliable manner, such that the fluorescent X-ray intensities from the constituent elements can be measured as a function of the electron incidence direction, with the particular systematic reflection row excited. Known as high-angular-resolution electron-channeling X-ray spectroscopy (HARECXS), this technique enables us to derive the impurity/dopant occupancies. More generally, it can also clarify the degree of cation mixing (anti-sites) of the host atoms, by comparing the experimental beam-rocking curves with theoretical simulations [4–7]. An extension of this technique, high-angular-resolution electron-channeling electron spectroscopy (HARECES), records the electron energy loss spectra (EELS) instead of EDX [8], thereby elucidating the local chemical states of a given element in different nearest-neighbor atomic environments. In these studies, a multivariate curve resolution (MCR) technique is crucial for separating the overlapping site-specific electron-energy-loss near-edge structures (ELNES) in the angle-dependent spectral data set. Our research group has demonstrated such site-specific EELS measurements in several crystalline materials [9–11].

Ni-substituted lithium manganese oxide spinel ($LiNi_xMn_{2-x}O_4$, space group: *Fd*-3*m*) is one of the most promising positive electrode materials for rechargeable lithium ion batteries, because of its higher operating voltage and lower toxicity and cost. Knowledge of the atomic configuration and valence states of the cations in an electrode material is crucial for improving its performance, such as the Li^+ ion mobility, C-rate dependent cycling stability, and charge-discharge capacity [12]. $LiNi_xMn_{2-x}O_4$ is considered to have an *fcc* framework of oxygen ions, with lithium ions occupying the tetrahedral (8a) sites, and manganese and nickel ions situated at the octahedral (16d) sites. X-ray diffraction (XRD) measurements of $LiNi_xMn_{2-x}O_4$ synthesized by a particular reaction path, however, revealed that some of the nickel ions occupied the tetrahedral rather than the octahedral sites [13]. The quantitative

analysis using this method remains controversial, however, because XRD analysis could be insensitive to the degree of cation mixing, particularly for multi-doped transition metal (TM) elements due to their close atomic numbers. Neutron diffraction is a more reliable method for such cases, though it is neither easy to use nor applicable to samples smaller than 1 micrometer. In this context, the HARECXS/HARECES methods can be promising alternatives.

It is generally believed that Mn in $LiNi_xMn_{2-x}O_4$ can be trivalent or tetravalent, depending on the amount of Ni-substitution and/or the loss of oxygen [12–15], whereas nickel remains divalent [13,16]. Although conventional EELS and X-ray photoelectron spectroscopy (XPS) measurements have been adopted to investigate the valence states of cations, these techniques only provide information averaged over atoms at different sites. Hence the relationship between the site occupancy and the valence state of the cations in $LiNi_xMn_{2-x}O_4$ remains unclear. The present study aims to clarify this relationship, by applying the suite of HARECXS and HARECES analyses to $LiNi_xMn_{2-x}O_4$ for x = 0–0.5, as well as a deliberately and excessively Ni-doped sample material (determined below as $Li_{0.21}Ni_{0.7}Mn_{1.64}O_{4-\delta}$). The degree of cation mixing between the tetrahedral and octahedral sites in the samples can be probed quantitatively by HARECXS. Then the site-dependent local electronic structures of the cationic TM elements can be investigated by the combined HARECXS and HARECES analysis.

Experimental procedures

Sample synthesis, characterization, and thin film preparation for transmission electron microscopy

Four different sample materials were prepared for the present study. A $LiMn_2O_4$ ($LiNi_xMn_{2-x}O_4$ with x = 0) single crystal was grown by the solvent evaporation flux method.

The $LiNi_{0.2}Mn_{1.8}O_4$ (x = 0.2) and $LiNi_{0.5}Mn_{1.5}O_4$ (x = 0.5) single crystals were synthesized without flux materials as described elsewhere [17, 18]. Finally, the excessively Ni-doped material was synthesized without flux materials from a 2:3:1 + α ($\alpha << 1$) molar mixture of LiOH, $MnCl_2$, and $NiCl_2$. This material is referred to as "x = 0.7" hereafter.

The samples were first characterized by single-crystal XRD at room temperature, using Mo-K_α radiation in a Rigaku R-AXIS RAPID-II diffractometer (operating conditions: 50 kV, 40 mA) equipped with a curved imaging plate detector. The chemical compositions of the Li, Mn and Ni cations were determined by inductively coupled plasma-atomic emission spectroscopy (ICP-AES, Thermo-Fisher Scientific, iCAP6500 Duo View). The acid solutions used for ICP-AES were prepared by melting the single crystals with sodium pyrosulfate, and then dissolving the mixture in hydrochloric acid.

The morphology observations of the single crystals, and preparation of thin films (50–150 nm thick) for transmission electron microscopy (TEM) were performed with a focused ion beam (FIB) equipped with a scanning electron microscope (SEM, FEI Helios NanoLab^{TM} 600). An FEI TITAN80-300 TEM equipped with an EDAX r-TEM/SuperUTW EDX system and a Gatan GIF Tridiem EELS system were used in the TEM-diffraction mode at an accelerating voltage of 200 kV to acquire electron diffraction pattern (EDP), EDX, and EELS data. The approximate size of the electron-illuminated area on the TEM specimens was a few hundred nanometers in diameter.

HARECXS/HARECES measurements

The tetrahedral and octahedral sites in the spinel structure are located in alternate planes in the stacked {400} lattice. The peak positions of the Bloch wave intensities propagating along the planes containing the tetrahedral or octahedral sites can vary, according to the subsequent excitation of the h 0 0 reflections by tilting the incident beam in the direction of the 400

systematic row reflections. HARECXS and HARECES measurements were carried out by tilting the incident beam with a systematic excitation of −4**g** to 4**g**, where **g** = 4 0 0. Data of characteristic X-ray up to 20 keV were acquired, and their recording times were 10–50 s per tilting angle. The O-, Mn-, and Ni-K_α line intensities were extracted from the dataset. The sequential EDX/EELS data acquisitions with successive incident beam tilting were carried out using the scripting program TIA running on the TEM imaging and analysis platform. This open source software enabled full digital control of the FEI TEMs and attached detectors.

The orientation-dependent X-ray emissions as functions of the tilting angle were calculated using the ionization cross-section calculator (ICSC) code, based on the dynamical electron diffraction theory incorporating inelastic scattering to yield the fluorescent X-ray and energy loss cross-sections [19–22]. When cation mixing takes place between the tetrahedral and octahedral sites, the experimental rocking curves of the TM elements should be reproduced by the ICSC code if the mixed-site occupancies for the TM sites are described in the input structure file. In the present study, we first assumed a linear combination of the theoretical rocking curves from the tetrahedral and octahedral sites, with the corresponding occupation probability as the weighting coefficient for each component. The probabilities can be evaluated by the linear least-squares fit where the theoretical rocking curves of the two TM sites are calculated, assuming that manganese alone occupies the octahedral sites for x = 0, 0.2, and 0.5 as the initial structure. For x = 0.7, we started with the structure in which manganese or nickel occupied the octahedral sites alone, and an iterative procedure similar to the case above was applied till convergence was obtained. This fitting scheme worked well and rapidly converged to the final solution, because the Bloch wave field in the material remained almost unchanged by the occupancy variation, due to the very similar scattering power between manganese and nickel. The data points for all these curves were normalized by the intensity measured in the kinematical condition, ±4**g**.

The $L_{2,3}$ ELNES of the TM elements were recorded at the same time as the HARECXS measurement, at a detector dispersion of 0.1 eV/channel, energy resolution of about 1.0 eV as estimated by the full width at half maximum (FWHM) of the zero-loss peak, collection semi-angle of 1.5–4.9 mrad, and beam convergence semi-angle of ~0.3 mrad. The detector entrance aperture was located at 1.0|**g**| away from the origin along the 400 Kikuchi line in the TEM-diffraction mode to enhance the localization effect of the core-loss spectra [8, 10].

HARECES analysis using HARECXS data

In a set of angular-resolved EELS of the TM elements occupying partly tetrahedral and octahedral sites, each EEL spectrum is expressed by a linear combination of two EEL spectra, one from the tetrahedral site and the other from the octahedral site. The weight of these components varies with the diffraction conditions. The relationship among the experimental spectral set, the spectral components from the two sites, and their weight coefficients is expressed by the following matrix equation:

$$\mathbf{X} = \mathbf{SC} + \mathbf{R}, \qquad (1)$$

where **X**, **S**, **C**, and **R** are respectively $n \times m$, $n \times 2$, $2 \times m$, and $n \times m$ matrices, in which n is the number of EELS detector channels (in the energy-loss axis) used for the analysis and m is the number of steps in the incident beam direction axis. Each column of **X** is the experimental EEL spectrum at a specific incident direction. Similarly, the two columns of **S** correspond to the two EEL spectra from the tetrahedral and octahedral sites. The i-th column of **C** corresponds to the weight coefficients of the tetrahedral and octahedral sites, for the experimental spectrum at the i-th incident beam direction. Finally, **R** is the residual matrix, which contains the statistical noise alone when the appropriate **S** and **C** matrices are found. If each component spectrum in **S** is normalized by its integrated intensity, each matrix element in **C** should be proportional to the product of the total cross-section of the core-loss of either

site at the specified diffraction condition, and the relative occupancy of the site.

In previous studies [9–11, 23], the matrix equation (1) has been solved by applying the MCR technique for materials with known site occupancies (N_{site}). In the present study, however, the HARECXS data simultaneously measured with HARECES directly provide the N_{site} values. To relate the site occupancies to the elements in the matrix **C**, the total core-loss cross-section for each site, σ_{site}, in the present experimental geometry is needed. σ_{site} is obtained by integrating the following second-order differential equations for a specimen with thickness t, based on the dynamical diffraction theory described in [24,25]:

$$\frac{\partial^2 \sigma_{site}}{\partial E \partial \Omega} \propto \sum_u \sum_{jj'll'} \sum_{gg'hh'} e^{i(q-q')\cdot u} T^{(jj'll')}(t) Y^{(jj'll')}_{gg'hh'} \frac{S_u(q,q',E)}{q^2 q'^2}, \quad (2)$$

with site = tet. or oct. for the tetrahedral and octahedral sites, respectively. Ω is the solid angle subtended by the EELS detector, $\boldsymbol{u}$ is the atomic position in the unit cell, and the superscripts j (l) and subscripts g (h) stand for the indices of the Bloch wave branches corresponding to the different dispersion surfaces for incoming (outgoing) electrons and the elastic scattering vectors excited by the incoming (outgoing) electrons, respectively. The term $e^{i(\boldsymbol{q}-\boldsymbol{q}')u}$ works as the structure factor and determines the atomic site-selectivity, where $\boldsymbol{q} = (\boldsymbol{k}^{(l)}_{\mathrm{out}} + \boldsymbol{h}) - (\boldsymbol{k}^{(j)}_{\mathrm{in}} + \boldsymbol{g})$ and $\boldsymbol{q}' = (\boldsymbol{k}^{(l')}_{\mathrm{out}} + \boldsymbol{h}') - (\boldsymbol{k}^{(j')}_{\mathrm{in}} + \boldsymbol{g}')$ are the momentum transfer vectors of the scattered electrons causing the interference. $T^{(jj'll')}(t)$ is a thickness-dependent function [26], $Y^{(jj'll')}_{gg'hh'}$ is a product of the Fourier coefficients of the incoming and outgoing Bloch waves, and $S_u(\boldsymbol{q},\boldsymbol{q}',E)$ is known as the mixed dynamical form factor (MDFF) for a single atom [27]. In case of small $\boldsymbol{q}$ and $\boldsymbol{q}'$—typically less than 1.0|**g**| [23]—the MDFF can be expressed by the simple inner product of $\boldsymbol{q}$ and $\boldsymbol{q}'$ within the dipole transition approximation [25]. Each element C_{site} in **C** is consequently expressed by the following normalized weight coefficient at each diffraction condition (tilting angle of the incident beam):

$$C_{tet} = \frac{N_{tet}\sigma_{tet}}{N_{tet}\sigma_{tet} + N_{oct}\sigma_{oct}}. \quad (3)$$

The C_{site} values in some spinel-type TM oxides with known N_{site} have been extracted by MCR and found to be quantitatively comparable with the theoretical values based on inelastic scattering cross-section calculation [23]. Since the **C** matrices can be estimated by the theoretical site-specific inelastic scattering cross-sections and experimental N_{site} using HARECXS, Eq. (1) can be solved by simply applying a multiple linear regression (MLR) method to extract the component spectra of the TM at the tetrahedral and octahedral sites.

Results and discussion

Material characterization

A SEM image of $LiNi_{0.5}Mn_{1.5}O_4$ (x = 0.5) is shown in Figure 1, with the inset showing <001> EDP. All the as-synthesized samples in this study exhibited morphologies very similar to those in Figure 1, i.e., agglomerates of single crystals having octahedral shapes with {111} facets, from a few to tens of micrometers in size. The XRD results of these samples showed sharp diffraction spots, all of which consistent with the cubic spinel structure (space group: *Fd*-3*m*). In the EDP of x = 0.5, super-lattice reflections were observed in addition to the fundamental lattice reflections. The super-lattice reflections are attributed to the ordering of Ni^{2+} and Mn^{4+} in the octahedral sites, which suggests the coexistence of the $P4_332$ phase in the single crystal. It was theoretically confirmed that the orientation-dependent X-ray intensities along the 400 systematic rows of reflections in *Fd*-3*m* and $P4_332$ structures behave in the same manner. Hence, all samples in the present study were examined by the same procedure.

The molar ratios of the cations determined by ICP-AES are tabulated in Table I. The molar ratios in the samples with x = 0–0.5 are close to the values based on the initial synthesis composition. The sample with x = 0.7 had a smaller amount of Li and larger amount of the TM elements compared to the expected chemical formulae, likely due to the partial

replacement of tetrahedral sites by the TM elements, as will be revealed in the next section. An oxygen deficiency was also confirmed for $x = 0.7$ from the lower relative intensity ratio between the O-K and Mn-$L_{2,3}$ ELNES. The nominal composition for $x = 0.7$ can be expressed as $Li_{0.2}Ni_{0.7}Mn_{1.6}O_{4-\delta}$. Even though this sample may not be suitable for the rechargeable lithium ion battery, it is worthwhile to examine its cation-mixing behavior for comparison with the other samples.

Cationic site occupancies by HARECXS

Figure 2 shows the theoretical ionization cross sections (proportional to the X-ray emission intensities) of the O-K_α line and the Mn-K_α lines from the tetrahedral and octahedral sites as functions of the beam tilting angle, $k_x/|\mathbf{g}|$. k_x is the distance from the origin to the intersection between the Ewald sphere and the 100 axis in reciprocal space, and $k_x/|\mathbf{g}| = 1$ corresponds to the exact 400 Bragg condition. The Mn-K_α lines (not shown) behaved in almost the same way as the Ni-K_α lines. The angle-resolved ionization cross sections of manganese (nickel) at the octahedral sites and oxygen are broadly convex in the range of $-1 \leq k_x/|\mathbf{g}| \leq 1$, while manganese (nickel) at the tetrahedral sites exhibits a concave profile in the same range, with distinct peaks on both sides over the range of $\pm 1 \leq \pm k_x/|\mathbf{g}| \leq \pm 2$ (the double signs correspond).

The experimental HARECXS data obtained from the present samples are shown in Figs. 3(a)–(k), with the best-fit curves (solid lines) overlaid. Although the O-K_α data should be independent of cation mixing, they are included to illustrate the validity of theoretical simulation. The derived occupation probabilities for manganese and nickel in the tetrahedral and octahedral sites are tabulated in Table I. These values are averaged among the best-fit results obtained from several measurements, and their standard deviations among the measurement areas are also listed. The sixth and seventh columns of Table I are, respectively,

the residual sum of squares χ^2 between the experimental and theoretical beam-rocking curves as a measure of goodness-of-fit (GOF), and the noise level σ^2 estimated by the standard deviation between the experimental and low-pass filtered curves. It is thus implied that the present best-fit results mostly converged well to the level where χ^2/σ^2 is close to unity, which means that the fit results match the experimental data well.

In the samples with x = 0–0.5, the profiles for Mn- and Ni-K_α exhibit a similar trend in the primary peak at $-1 \le k_x/|\mathbf{g}| \le 1$, whereas the Mn-$K_\alpha$ profile of the sample with x = 0.7 exhibits a relatively lower intensity in the primary peak and distinct peaks at $k_x/|\mathbf{g}| \sim \pm 1.8$. These results suggest that manganese and nickel ions mostly occupy the octahedral sites for $0 \le x \le 0.5$, whereas the manganese ions also occupy tetrahedral sites for x = 0.7, as shown in Table I. In addition, the heights of the primary peaks of the Ni-K_α profiles for x = 0.2 and 0.5 are slightly smaller than those of the Mn-K_α profiles. This is quantitatively expressed as approximately 10% of the nickel ions occupying tetrahedral sites in the Ni-doped samples, which is consistent with a previous report [13]. In the x = 0.2 and 0.7 samples, not only Ni but also Mn atoms occupy the tetrahedral sites. Especially, in the x = 0.7 sample about one-third of the Mn atoms occupy the tetrahedral sites. This situation is similar to that in the Mn_3O_4 spinel, as expressed by the formula $[Mn]_{tet}[Mn_2]_{oct}O_4$.

Valence states of transition metal elements by simultaneous HARECXS/HARECES measurements

The average valence of the manganese ions in each sample was determined by comparing the Mn-$L_{2,3}$ (particularly Mn-L_3) ELNES with those of MnO_2 and Mn_3O_4 as reference materials, as shown at the top of Figs. 4(a) and 4(b), respectively. It has been shown that the Mn-$L_{2,3}$ spectrum in various natural minerals depends highly on its valence state, but exhibits the same basic edge shape with little variation in coordination number or site symmetry [28].

The Mn-$L_{2,3}$ ELNES of all the samples measured at non-localized condition (the EELS entrance aperture was set at the origin in the TEM-diffraction mode [8, 23]) are shown in Fig. 4(a). Since MnO_2 includes only Mn^{4+}, the Mn-$L_{2,3}$ ELNES at the top of Fig. 4(a) is the fingerprint spectrum for Mn^{4+}. The difference spectrum between the Mn-L_3 profile of each sample and MnO_2 is shown in Fig. 4(b) and compared with the Mn-L_3 profile of Mn_3O_4 at the top (broken line) as mixed Mn^{2+} and Mn^{3+} occupying the tetrahedral and octahedral sites, respectively. The Mn^{2+} and Mn^{3+} spectra are shown as solid lines, each extracted using the MCR method used in a previous paper [23]. The qualitative conclusion is that the valence states of the manganese ions should be a mixture of trivalent and tetravalent for $x = 0$, nearly all tetravalent for $x = 0.5$, and a mixture of di-, tri- and tetravalent for both $x = 0.2$ and 0.7. Since the HARECXS analysis in the previous section shows that the manganese ions occupied only the octahedral sites for $x = 0$, Mn^{3+} and Mn^{4+} should be randomly distributed among the octahedral sites, considering that no super-lattice reflections were observed in the EDP.

Let us examine the relationship between the cationic occupation sites and their valence states in more detail for the samples with $x = 0.2$ and 0.7. A series of the Mn-L_3 ELNES for $x = 0.7$, with the incident beam subsequently tilted under the condition with the 400 systematic row of reflections excited, and the Mn-K_α HARECXS rocking curves taken at the same time are shown in Fig. 5(a) and 5(b), respectively. Each HARECES curve in Fig. 5(a) is displaced along the vertical axis so that its baseline position corresponds to the position of the vertical axis in Fig. 5(b). It is seen in Fig. 5(a) that the peak near 639 eV (fingerprint of Mn^{2+}) is enhanced for $1 \leq k_x/|\mathbf{g}| \leq 2$, where the atomic planes including the tetrahedral sites are preferentially excited. On the other hand, the peak near 642 eV (fingerprint of Mn^{4+}) is dominant for $0 \leq k_x/|\mathbf{g}| \leq 1$, where the octahedral sites are preferentially excited. This tendency is the qualitative evidence for the correlation between the site occupancy and valence state of

the manganese ion. The Mn-L_3 ELNES for x = 0.7, selectively obtained for the tetrahedral and octahedral sites, were extracted by solving Eq. (1) and shown in Fig. 6(a), together with the reference divalent, trivalent, and tetravalent Mn-L_3 spectra. All the spectra were normalized by the respective integrated spectral intensities. The **C** matrix was prepared according to Eqs. (2) and (3) by the site occupancies derived from the HARECXS data (as discussed in the previous section) and the theoretical site-specific total cross sections using the analytical formula in the two-beam approximation, because the simulation results by the two-beam approximation and the fully dynamical many-beam calculation code [22] showed little difference in the range of $0.5 \leq k_x/|\mathbf{g}| \leq 1.5$. The spectral profile of Mn_{oct}-L_3 is in good agreement with that of Mn^{4+}, suggesting that the manganese ions at the octahedral sites are essentially tetravalent. On the other hand, the spectral profile of Mn_{tet}-L_3 is similar to that of Mn^{2+}, indicating that most of the manganese ions at the tetrahedral sites are divalent, with possibly a slight amount of other valence states. This reduced valence state is consistent with the oxygen deficiency of this sample compared to the other samples, judging from the lower relative intensity ratio of O-K/Mn-$L_{2,3}$. It should be noted that the spectral profile of the Mn_{tet}-L_3 is best fitted by the linear combination of Mn^{2+}- and Mn^{3+}-L_3 spectra with a ratio of 67:33.

Similar reasoning holds for the sample with x = 0.2 in Fig. 6(b), where the Mn-L_3 ELNES were also site-selectively extracted. The manganese ions at the octahedral sites are essentially tetravalent, as for x = 0.7. The spectral profile of Mn_{tet}-L_3 is best fitted by a linear combination of Mn^{2+}- and Mn^{3+}-L_3 spectra, with a ratio of 43:57. The presence of a significant amount of Mn^{3+} is consistent with previous reports [12, 13], where the potential-capacity profile of the $Li/LiNi_{0.2}Mn_{1.8}O_4$ battery cell exhibited a plateau around 4.1 V attributed to the oxidation reaction from Mn^{3+} to Mn^{4+}.

The Ni-$L_{2,3}$ ELNES measured at a non-channeling condition are shown in Fig 7. The L_2/L_3

intensity ratios and spectral profiles of all the samples are very similar to those of NiO, which exhibits typical divalent features. The spectral features were independent of the incident electron direction, suggesting that the valence state of the nickel ions is site-independent in the present samples.

The valence states of the cations, their fractions, and the net charges in the chemical formulae are also summarized in the far-right columns of Table I. These data show that the local charge neutrality condition is generally fulfilled (except the case for x = 0.7) within experimental accuracy, assuming fully occupied divalent oxygen sites and taking into account the 5–10% error in the composition and fractions of cations with different nominal charges in each sample. The net cation charge of x = 0.7 is significantly less than 8, which is attributable to its observed oxygen deficiency.

Concluding remarks

We investigated the atomic site occupancies and site-specific valence states of transition metal elements in $LiNi_xMn_{2-x}O_4$ (x = 0, 0.2 and 0.5) and excessively Ni-doped lithium manganese oxide, $Li_{0.2}Ni_{0.7}Mn_{1.6}O_{4-\delta}$ (x = 0.7), using HARECXS/HARECES associated with TEM equipped with EDX and EEL spectroscopic detectors. The obtained results are summarized as follows. (1) For x = 0.2–0.7, the nickel ions are divalent independent of the occupation sites, and 6–13% nickel ions occupy the tetrahedral anti-sites (lithium sites). (2) For x = 0, manganese ions occupy the octahedral sites alone, and are either trivalent or tetravalent, presumably to maintain local charge neutrality. (3) In the Ni-doped samples, manganese occupies both the octahedral and tetrahedral sites, being tetravalent in the octahedral sites. Manganese is either divalent or trivalent in the tetrahedral sites for x = 0.2 and 0.7, and nearly all situated in the octahedral sites as the tetravalent species for x = 0.5. The net charge in each Ni-doped sample satisfies local charge neutrality requirements within

experimental accuracy.

The present simultaneous HARECXS/HARECES data acquisition and analysis with dynamical electron diffraction theories provide a simple, practical, and automated measurement methodology to obtain quantitative information specific to both the element and site for the constituent elements in a wide range of important materials. This technique does not require state-of-the-art instruments such as expensive aberration-corrected TEMs or large-scale facilities with neutron diffraction and synchrotron radiation sources. It requires a sample with only a small (<1 μm) mono-crystalline grain size and easily producible thickness (> 50 nm) which is much higher than that required for atomic resolution observation. This method is complementary with other site/element selective analysis methods, in the sense that the atomic structure of the sample of interest must be known in advance and should not significantly change with its composition and site occupancy characteristics.

Funding

A part of this work was supported by Grants-in-Aid on Innovative Areas “Nano Informatics” (Grant No. 25106004) and Kiban-kenkyu A (Grant No. 26249096) from the Japan Society for the Promotion of Science.

References

1. Taftø J, Spence J C H (1982) Atomic site determination using the channeling effect in electron-induced X-ray emission. *Ultramicroscopy* **9**, 243–248.
2. Spence J C H, Taftø J (1983) ALCHEMI: a new technique for locating atoms in small crystals. *J. Microsc.* **130**, 147–154.
3. Shindo D, Hirabayashi M, Kawabata T, Kikuchi M (1986) A channeling enhanced microanalysis on niobium atom location in an Al-43%Ti-2%Nb intermetallic compound.

J. Electron Microsc. **35**, 409–414.

4. Soeda T, Matsumura S, Kinoshita C, Zaluzec N J (2000) Cation disordering in magnesium aluminate spinel crystals induced by electron or ion irradiation. *J. Nucl. Mater.* **283**, 952–956.
5. Yasuda K, Yamamoto T, Shimada M, Matsumura S, Chimi Y, Ishikawa N (2006) Atomic structure and disordering induced by 350 MeV Au ions in $MgAl_2O_4$. *Nucl. Instr. and Meth. B* **250**, 238–244.
6. Morimura T, Hasaka M (2005) Electron channeling X-ray microanalysis for partially filled skutterudite structure. *Micron* **36**, 429–435.
7. Morimura T, Hasaka M (2006) ALCHEMI for coexistent Heusler and half-Heusler phases in $TiNi_{1.5}Sn$. *Ultramicroscopy* **106**, 553–560.
8. Taftø J, Krivanek O L (1982) Site-specific valence determination by electron energy-loss spectroscopy. *Phys. Rev. Lett.* **48**, 560–563.
9. Yamamoto Y, Tatsumi K, Muto S (2007) Site-selective electronic structure of aluminum in oxide ceramics obtained by TEM-EELS analysis using the electron standing-wave method. *Mater. Trans.* **48**, 2590–2594.
10. Tatsumi K, Muto S (2009) Local electronic structure analysis by site-selective ELNES using electron channeling and first-principles calculations. *J. Phys. Condens. Matt.* **21**, 104213.
11. Tatsumi K, Muto S, Nishida I, Rusz J (2010) Site-specific electronic configurations of Fe 3*d* states by energy loss by channeled electrons. *Appl. Phys. Lett.* **96**, 201911.
12. Zhong Q, Bonakdarpour A, Zhang M, Gao Y, Dahn J R (1997) Synthesis and electrochemistry of $LiNi_xMn_{2-x}O_4$. *J. Electrochem. Soc.* **144**, 205–213.
13. Wei Y, Kim K B, Chen G (2006) Evolution of the local structure and electrochemical properties of spinel $LiNi_xMn_{2-x}O_4$ ($0 \leq x \leq 0.5$). *Electrochim. Acta* **51**, 3365–3373.

14. Kim J H, Myung S T, Yoon C S, Kang S G, Sun Y K (2004) Comparative study of $LiNi_{0.5}Mn_{1.5}O_{4-\delta}$ and $LiNi_{0.5}Mn_{1.5}O_4$ cathodes having two crystallographic structures: *Fd*-3*m* and $P4_332$. *Chem. Mater.* **16**, 906–914.
15. Ma L W, Chen B Z, Shi X C, Zhang W, Zhang K (2010) Stability and Li^+ extraction/absorption properties of $LiM_xMn_{2-x}O_4$ (M = Ni, Al, Ti; $0 \leq x \leq 1$) in aqueous solution. *Colloids and Surfaces A* **369**, 88–94.
16. Amine K, Tukamoto H, Yasuda H, Fujita Y (1997) Preparation and electrochemical investigation of $LiMn_{2-x}Me_xO_4$ (Me: Ni, Fe, and x = 0.5, 1) cathode materials for secondary lithium batteries. *J. Power Sources* **68**, 604–608.
17. Akimoto J, Takahashi Y, Gotoh T, Mizuta S (2001) Single crystal growth of the spinel-type $LiMn_2O_4$. *J. Cryst. Growth* **229**, 405–408.
18. Takahashi Y, Sasaoka H, Kuzuo R, Kijima N, Akimoto J (2006) A low-temperature synthetic route and electrochemical properties of micrometer-sized $LiNi_{0.5}Mn_{1.5}O_4$ single crystals. *Electrochem. Solid-state Lett.* **9**, A203–A206.
19. Yoshioka H (1957) Effect of inelastic waves on electron diffraction. *J. Phys. Soc. Jpn.* **12**, 618–628.
20. Humphreys C J (1979) The scattering of fast electrons by crystals. *Rep. Prog. Phys.* **42**, 1825–1887.
21. Allen L J, Josefsson T W (1995) Inelastic scattering of fast electrons by crystals. *Phys. Rev. B* **52**, 3184–3198.
22. Oxley M P, Allen L J (2003) ICSC: a program for calculating inelastic scattering cross sections for fast electrons incident on crystals. *J. Appl. Cryst.* **36**, 940–943.
23. Tatsumi K, Muto S, Rusz J (2013) Energy loss by channeled electrons: A quantitative study on transition metal oxides. *Microsc. Microanal.* **19**, 1586–1594.
24. Saldin D K, Rez P (1987) The theory of the excitation of atomic inner-shells in crystals

by fast electrons. *Phil. Mag. B* **55**, 481–489.

25. Schattschneider P, Nelhiebel M, Schenner M, Grogger W, Hofer F (1996) Diffraction effects in inner-shell ionization edges. *J. Microsc.* **183**, 18–26.
26. Rusz J, Rubino S, Schattschneider P (2007) First-principles theory of chiral dichroism in electron microscopy applied to 3*d* ferromagnets. *Phys. Rev. B* **75**, 214425.
27. Kohl H, Rose H (1985) Theory of image formation by inelastically scattered electrons in the electron microscope. *Adv. Electron. Electron Phys.* **65**, 173–227.
28. Garvie L A J, Craven A J, Brydson R (1994) Use of electron-energy loss near-edge fine structure in the study of minerals. *Amer. Mineralog.* **79**, 411–425.

Table I. Summary of the quantitative analysis results in the study. Columns from left to right: *x* in the nominal composition in $Li_yNi_xMn_{2-x}O_{4-\delta}$, atomic elements, molar ratios of cations obtained by ICP-AES, the site distribution ratio of the tetrahedral and octahedral sites and its accuracy with standard deviation (STD) obtained by HARECXS analysis. χ^2 and σ^2 represent the goodness-of-fit (GOF) with the experimental values and averaged experimental noise level, respectively. The net cationic charge estimated by the cation valence states in each *x* is shown in the right-most column. The values in the parentheses in the penultimate column stand for the estimated error in the last digit of each value.

	ICP-AES analysis		HARECXS results					HARECXS/HARECES and EELS results		Net cationic charge
	Chemical composition		Site distribution ratio [%]		STD [%]	χ^2 [$\times10^{-3}$] (GOF)	σ^2 [$\times10^{-3}$]	Ionic composition		
x = 0	Li	0.89	-	-	-	-	-	Li^+	0.89(5)	8.2
	Mn	1.98	Tet.	0	0	1.2	1.4	-	-	
			Oct.	100				Mn^{3+}	0.63(8)	
								Mn^{4+}	1.35(8)	
x = 0.2	Li	1.20	-	-	-	-	-	Li^+	1.20(5)	8.4
	Mn	1.72	Tet.	8	3	1.1	0.64	Mn^{2+}	0.05(4)	
								Mn^{3+}	0.09(4)	
			Oct.	92				Mn^{4+}	1.58(1)	
	Ni	0.23	Tet.	13	12	3.6	4.1	Ni^{2+}	0.23(5)	
			Oct.	87						

	Li	1.02	-	-	-	-	-	Li^+	1.02(5)	
$x = 0.5$	Mn	1.52	Tet.	2	2	1.9	1.4	NA		7.9
			Oct.	98				Mn^{4+}	1.49(4)	
	Ni	0.48	Tet.	11	5	2.3	1.8	Ni^{2+}	0.48(5)	
			Oct.	89						
	Li	0.21	-	-	-	-	-	Li^+	0.21(5)	
$x = 0.7$	Mn	1.64	Tet.	30	4	0.85	0.49	Mn^{2+} Mn^{3+}	0.30(4) 0.19(4)	7.3
			Oct.	70				Mn^{4+}	1.15(4)	
	Ni	0.70	Tet.	6	5	1.5	1.2	Ni^{2+}	0.70(5)	
			Oct.	94						

Figure legends

Fig. 1. SEM image showing the typical morphology of $LiNi_{0.5}Mn_{1.5}O_4$ particles. Inset: the <001> electron diffraction pattern from its TEM specimen.

Fig. 2. Simulated HARECXS curves of Mn and O in $LiNi_{0.5}Mn_{1.5}O_4$ under successive diffraction conditions along the 400 systematic row of reflections, with an accelerating voltage of 200 kV, sample thickness of 120 nm, and 17 beams incorporated in the calculations along the systematic row.

Fig. 3. Experimental HARECXS data (solid circles with error bars) and their best fit curves (solid lines) for Mn-K_α, Ni-K_α, and O-K_α (from left to right) for the samples with x = 0, 0.2, 0.5, and x = 0.7 (from top to bottom). The error bars were estimated by the square root of the residual sum of squares between the data points and their median-filtered curve (window width = 3).

Fig. 4. (a) From top to bottom: Mn-$L_{2,3}$ ELNES of MnO_2, $LiNi_xMn_{2-x}O_4$ (x = 0, 0.2 and 0.5), and $Li_{0.2}Ni_{0.7}Mn_{1.6}O_{4-\delta}$ (x = 0.7), obtained under non-channeling conditions. (b) Top: Mn-L_3 ELNES of Mn_3O_4 (broken line) with the divalent (tetrahedral site) and tetravalent (octahedral site) components (solid lines) separated by the MCR method overlaid. Second from the top to bottom: the difference spectra between the Mn-L_3 ELNES of x = 0–0.7 and that of MnO_2. The energy-loss axis was calibrated so that the main peak position of Mn^{4+} (MnO_2) at 642 eV coincides with that of x = 0–0.7.

Fig. 5. (a) A set of Mn-L_3 HARECES for x = 0.7 with the incident beam tilted in the range $0 \leq k_x/g_{400} \leq 3$. Thick gray lines are the expected primary peak positions from Mn^{2+} and Mn^{4+},

respectively, as a visual guide. (b) HARECXS data of Mn-K_α concurrently taken with the HARECES data in (a).

Fig. 6. Site-specific spectra (black solid lines) of Mn-L_3 for the resolved octahedral (top: Mn_{oct}-L_3) and tetrahedral sites (bottom: Mn_{tet}-L_3) for (a) x = 0.7 and (b) x = 0.2. The Mn-L_3 ELNES of MnO_2 (Mn^{4+}: grey solid lines on top) is overlaid over each Mn_{oct}-L_3, and the reference spectra of Mn^{2+} and Mn^{3+} (solid thin lines) are also overlaid over Mn_{tet}-L_3 for comparison. Each spectrum was normalized by its integrated intensity. The grey solid lines at the bottom are the best fit curves to Mn_{tet}-L_3 by the two spectra (solid thin lines), with weights described in text.

Fig. 7. From top to bottom: Ni-$L_{2,3}$ ELNES of NiO, $LiNi_xMn_{2-x}O_4$ (x = 0.2, 0.5), and $Li_{0.2}Ni_{0.7}Mn_{1.6}O_{4-\delta}$ recorded under non-channeling conditions.

Figure 1

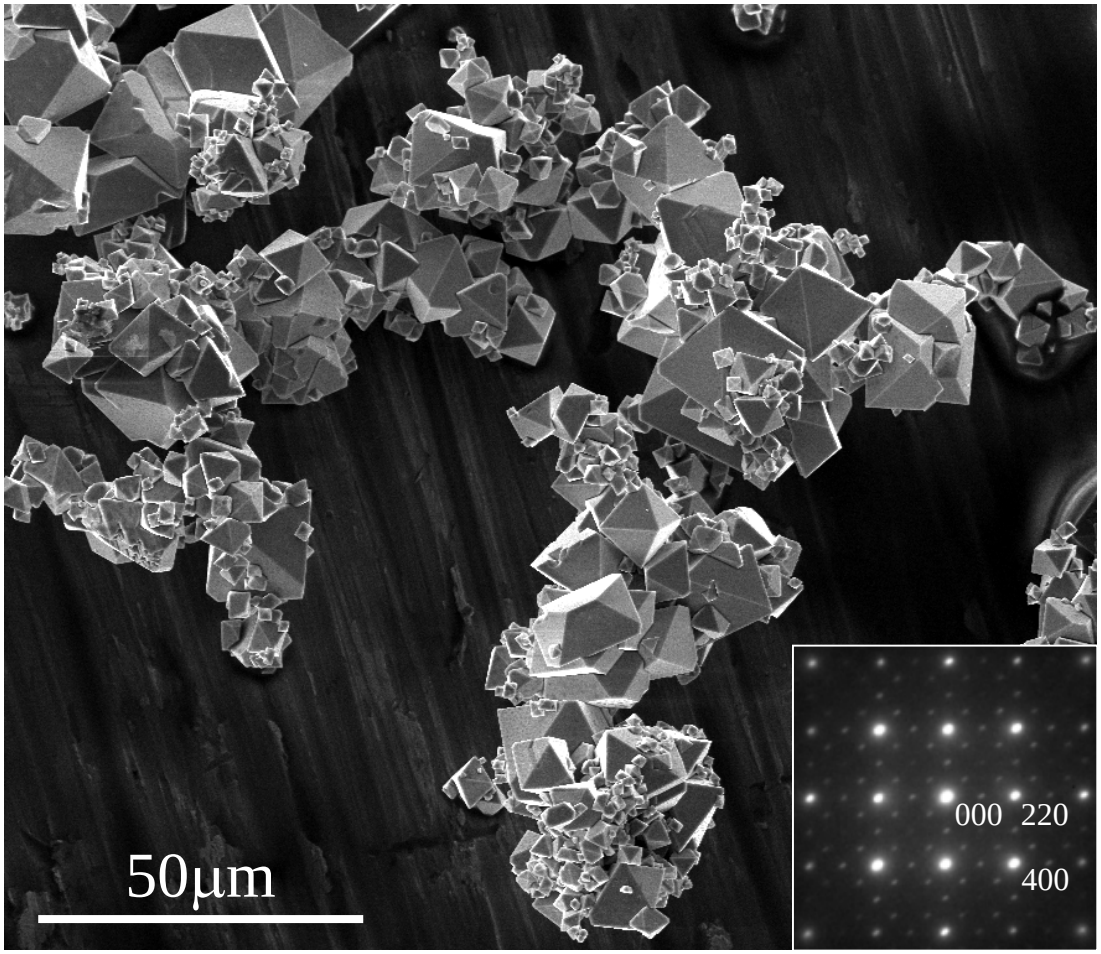

Figure 2

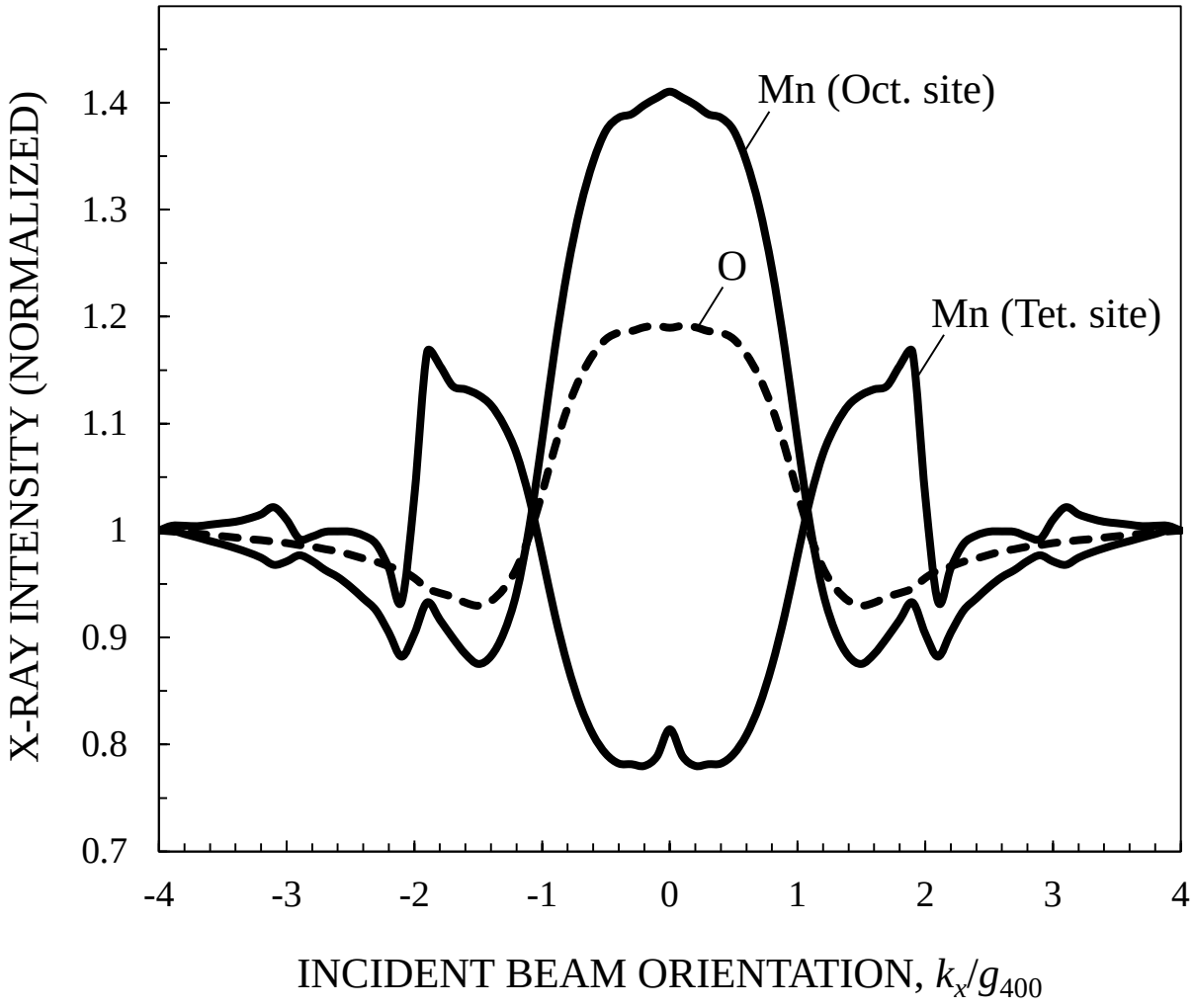
Mn (Oct. site)
O
Mn (Tet. site)
X-RAY INTENSITY (NORMALIZED)
1.4
1.3
1.2
1.1
1
0.9
0.8
0.7
-4
-3
-2
-1
0
1
2
3
4
INCIDENT BEAM ORIENTATION, k_x/g_{400}

Figure 3

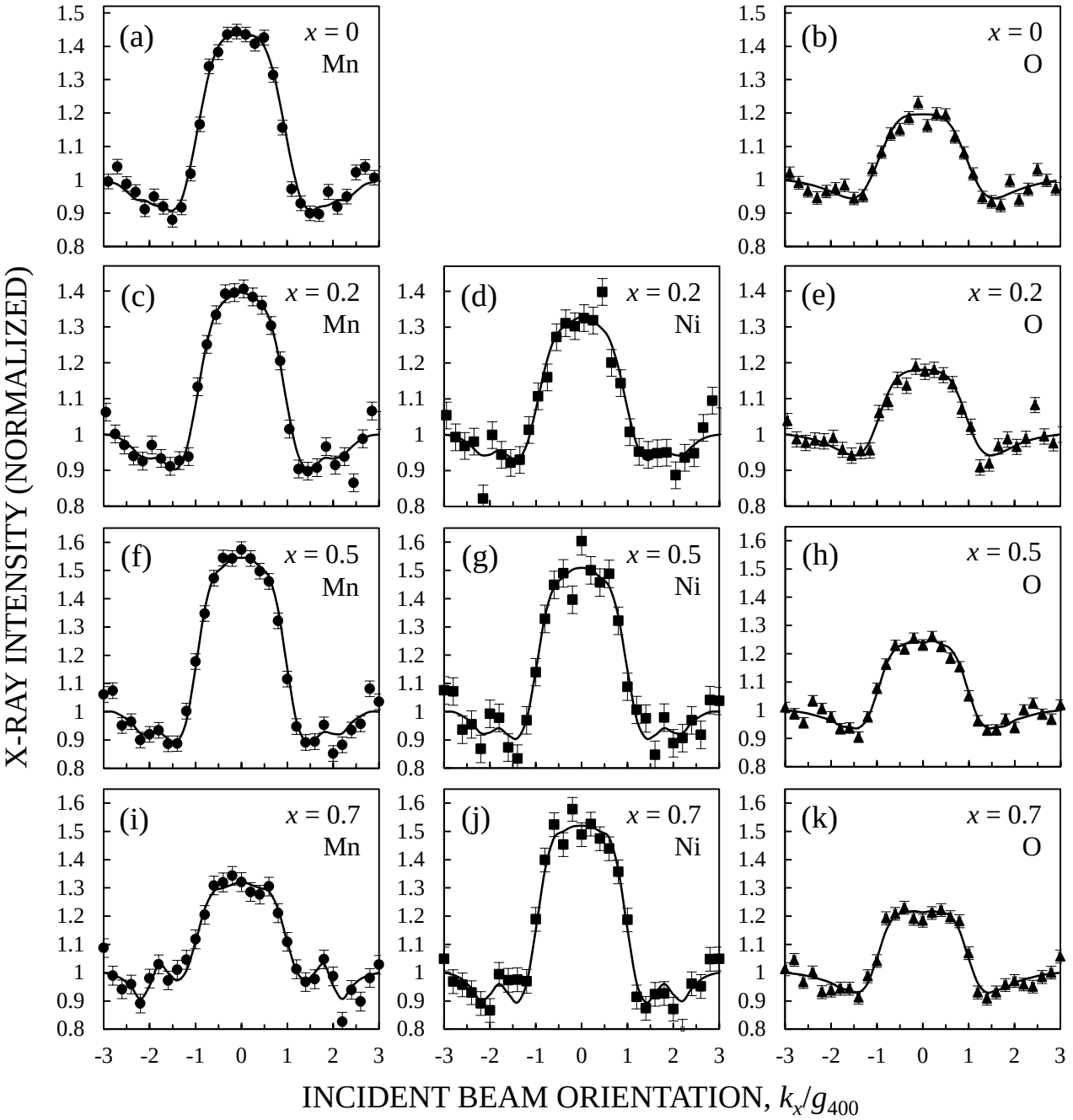
(a) x = 0 Mn
(b) x = 0 O
(c) x = 0.2 Mn
(d) x = 0.2 Ni
(e) x = 0.2 O
(f) x = 0.5 Mn
(g) x = 0.5 Ni
(h) x = 0.5 O
(i) x = 0.7 Mn
(j) x = 0.7 Ni
(k) x = 0.7 O
X-RAY INTENSITY (NORMALIZED)
INCIDENT BEAM ORIENTATION, k_x/g_{400}

Figure 4

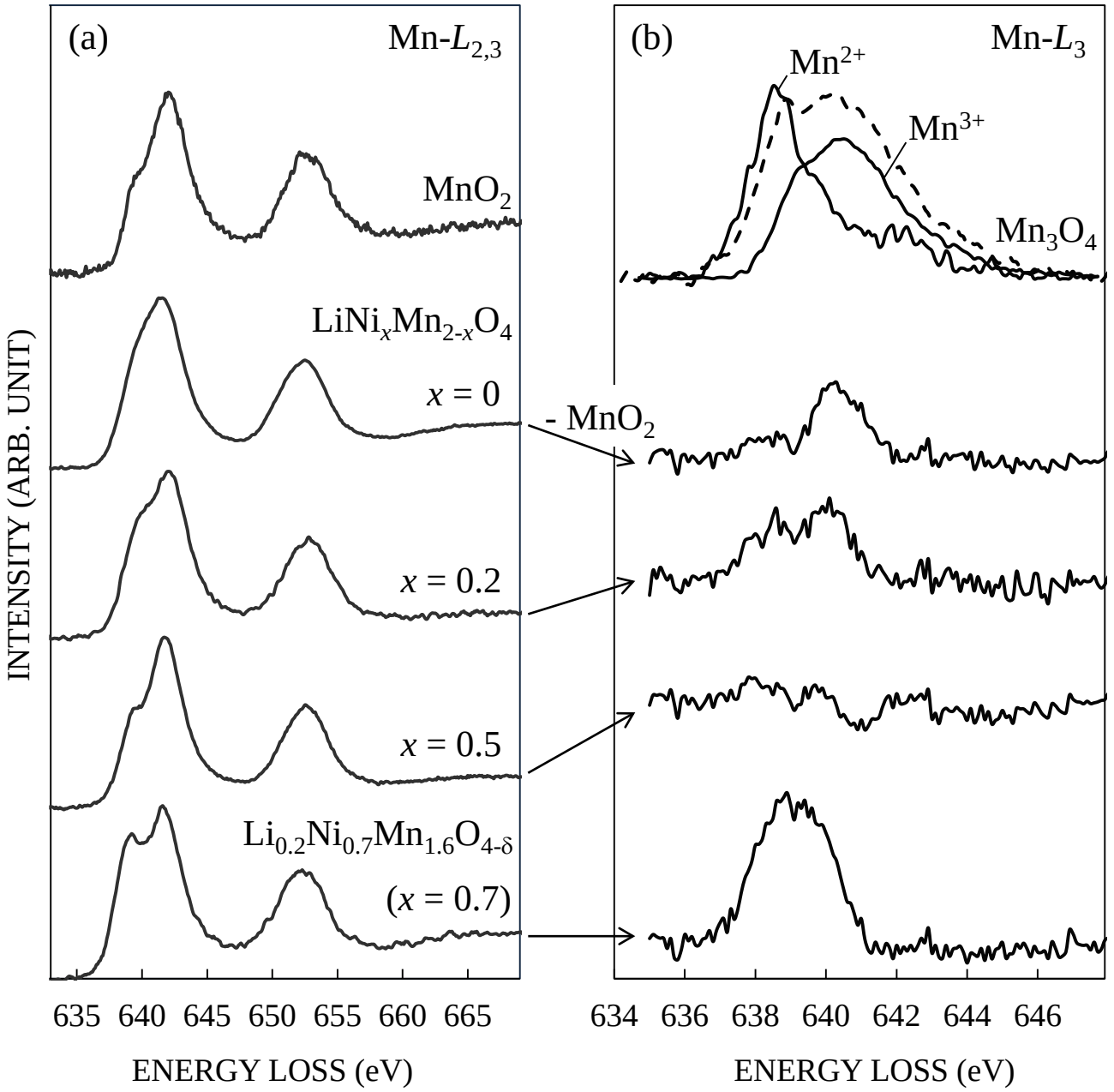
(a)
Mn-$L_{2,3}$
MnO_2
$LiNi_xMn_{2-x}O_4$
x = 0
x = 0.2
x = 0.5
$Li_{0.2}Ni_{0.7}Mn_{1.6}O_{4-\delta}$
(x = 0.7)
INTENSITY (ARB. UNIT)
635 640 645 650 655 660 665
ENERGY LOSS (eV)
(b)
Mn-L_3
Mn^{2+}
Mn^{3+}
Mn_3O_4
- MnO_2
634 636 638 640 642 644 646
ENERGY LOSS (eV)

Figure 5

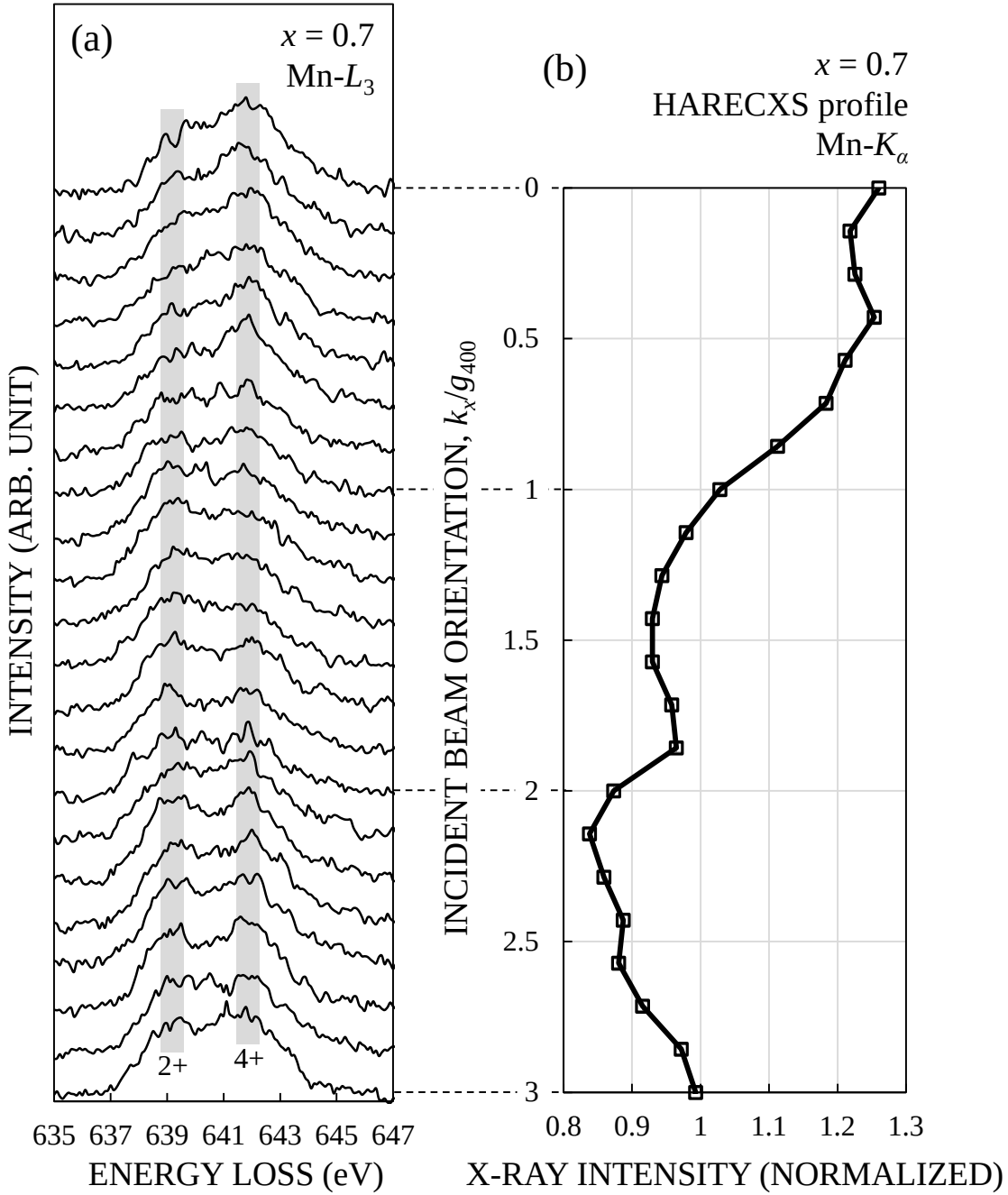
(a)
x = 0.7
Mn-L_3
2+
4+
INTENSITY (ARB. UNIT)
635 637 639 641 643 645 647
ENERGY LOSS (eV)
(b)
x = 0.7
HARECXS profile
Mn-K_α
INCIDENT BEAM ORIENTATION, k_x/g_{400}
0
0.5
1
1.5
2
2.5
3
0.8 0.9 1 1.1 1.2 1.3
X-RAY INTENSITY (NORMALIZED)

Figure 6

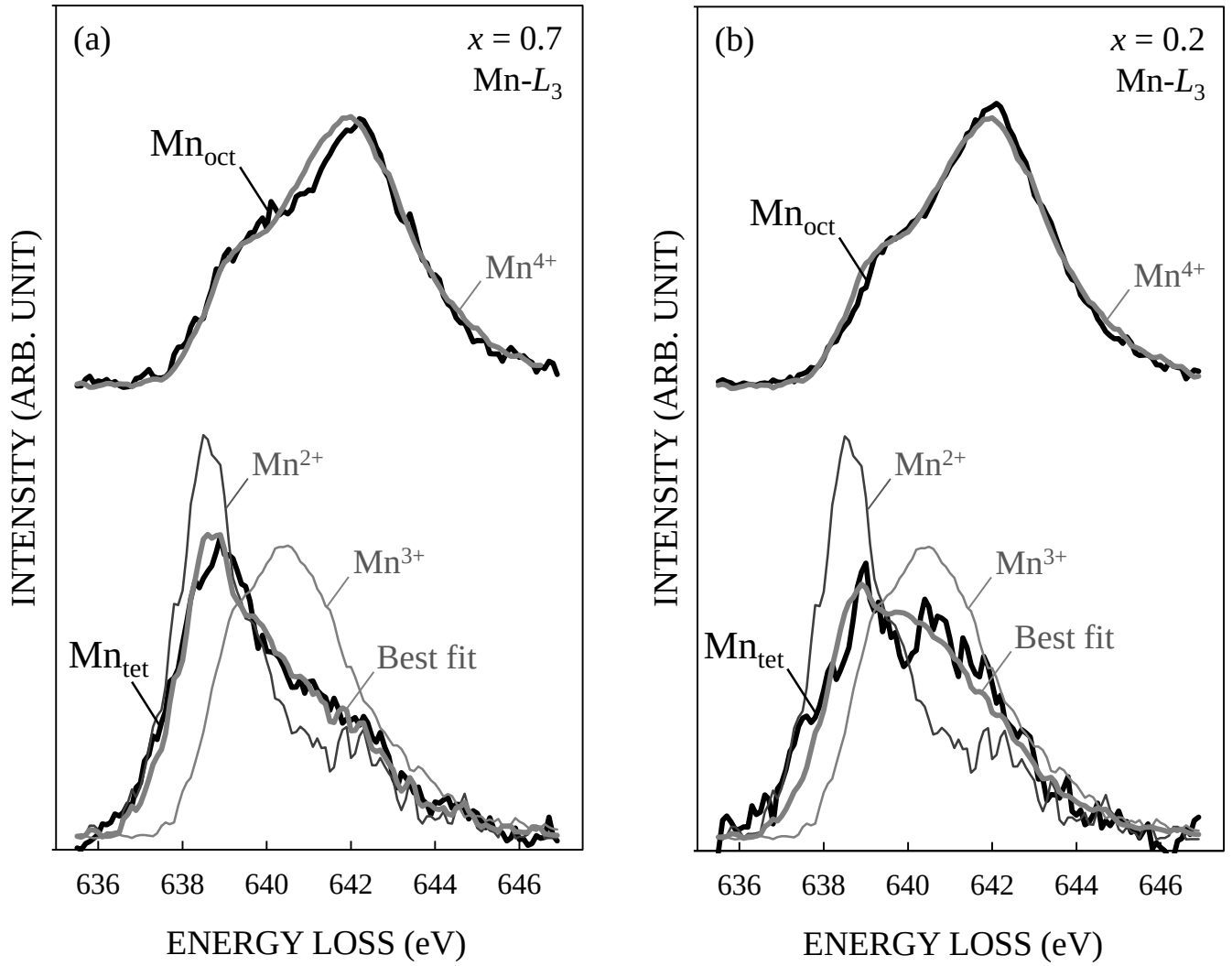
(a)
x = 0.7
Mn-L3
Mnoct
Mn4+
Mn2+
Mn3+
Mntet
Best fit
INTENSITY (ARB. UNIT)
636
638
640
642
644
646
ENERGY LOSS (eV)
(b)
x = 0.2
Mn-L3
Mnoct
Mn4+
Mn2+
Mn3+
Mntet
Best fit
INTENSITY (ARB. UNIT)
636
638
640
642
644
646
ENERGY LOSS (eV)

Figure 7

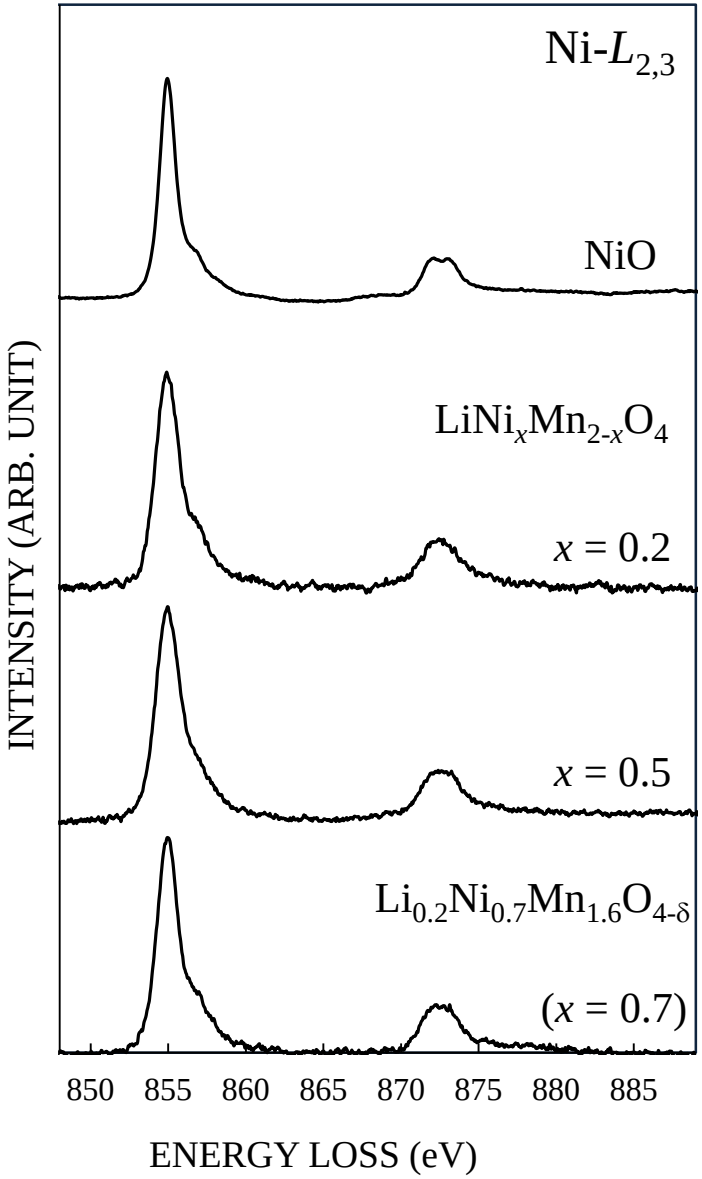
Ni-$L_{2,3}$
NiO
$LiNi_xMn_{2-x}O_4$
x = 0.2
x = 0.5
$Li_{0.2}Ni_{0.7}Mn_{1.6}O_{4-\delta}$
(x = 0.7)
INTENSITY (ARB. UNIT)
850 855 860 865 870 875 880 885
ENERGY LOSS (eV)